



Article

Estimation of Moist Atmospheric Profiles from Refraction and Attenuation Measurements by Using Centimeter and Millimeter Wave Links between LEO Satellites

Zhihua Zhang ^{1,2}, Xin Wang ^{1,*} and Daren Lyu ^{1,2}

¹ Key Laboratory of Middle Atmospheric and Global Environment Observation, Institute of Atmospheric Physics, Chinese Academy of Sciences, Beijing 100029, China

² University of Chinese Academy of Sciences, Beijing 100049, China

* Correspondence: wangx2003@mail.iap.ac.cn

Abstract: Microwave occultation using centimeter and millimeter wave links between low Earth orbit (LEO) satellites provide a potential way to estimate the moist atmospheric profiles based on refraction and attenuation measurements, which is called the LEO-LEO microwave occultation (LMO) technique. It has not yet been implemented in orbit. In this paper, we analyzed the attenuation properties at different heights of centimeter and millimeter waves based on simulations. The observing capabilities with different frequency combinations at the X, K, and M bands were analyzed. The results show that LMO may improve the retrieval accuracy of bending angles above 35 km. By using several appropriate frequencies at the X+K+M band, water vapor profiles from the near-surface to the lower stratosphere (~24 km) can be obtained. When the M-band frequencies were added, the temperature retrieval accuracy does not change obviously, but the accuracy of water vapor retrieval can significantly improve above 15 km, especially at about 17–24 km, and the RMS errors decrease from over 20% to less 10%. For promoting the LMO mission in the real world, a frequency combination at the X+K band is proposed, which can provide the potential to observe the temperature profiles at about 2.5–50 km and water vapor profiles at about 2.5–15 km accurately under clear and cloudy conditions. This study demonstrates that LMO can greatly extend the capabilities of the radio occultation technique and improve our ability to measure the moist atmospheric profiles globally.

Keywords: LEO-LEO occultation; microwave; attenuation; water vapor profile



Citation: Zhang, Z.; Wang, X.; Lyu, D. Estimation of Moist Atmospheric Profiles from Refraction and Attenuation Measurements by Using Centimeter and Millimeter Wave Links between LEO Satellites. *Remote Sens.* **2023**, *15*, 391. <https://doi.org/10.3390/rs15020391>

Academic Editors: Fei Xie, Zheng Sheng and Ji Zhou

Received: 30 November 2022

Revised: 22 December 2022

Accepted: 30 December 2022

Published: 8 January 2023



Copyright: © 2023 by the authors. Licensee MDPI, Basel, Switzerland. This article is an open access article distributed under the terms and conditions of the Creative Commons Attribution (CC BY) license (<https://creativecommons.org/licenses/by/4.0/>).

1. Introduction

Global climate change is one of the major challenges in the world. The sixth assessment report of the Intergovernmental Panel on Climate Change (IPCC) in 2021 announced that the global average temperature increase in this century should not exceed 2 degrees compared to the pre-industrial revolution and that every effort should be made not to exceed 1.5 degrees [1]. Water vapor is an important factor in monitoring the global water cycle and is one of the dominant greenhouse gases contributing to global warming. Its extreme sensitivity to temperature is reflected in the several orders of magnitude change in concentration from the surface to the upper stratosphere [2,3]. Small amounts of water vapor in the upper troposphere have a large effect on surface temperature through radiative forcing [4]. The uncertainty connected with water vapor in the upper troposphere and the lower stratosphere can cause great uncertainty when predicting global warming [5]. Therefore, an accurate and high-resolution knowledge of the temporal and spatial water vapor distributions is desirable. However, a significant challenge in measuring water vapor is its wide range of concentrations and scales [6,7]. Water vapor observations must be unbiased and able to capture all changes in clear and cloudy conditions globally [8,9].

The LEO-LEO cross-link radio occultation is an active remote sensing system that uses centimeter and millimeter (cm and mm) wavelength links between low Earth orbit (LEO)

satellites to measure the vertical profiles of water vapor, temperature, pressure, and density in the Earth's atmosphere [8]. The LEO-LEO microwave occultation (LMO) concept is a new occultation technique proposed in the late 1990s based on global navigation satellite system (GNSS) radio occultation (RO) [10]. The GNSS-LEO radio occultation (GRO) technique uses receivers on LEO satellites to receive the L-band signals from GNSS transmitters [11,12]. The highest quality of the retrieved variables is achieved in the upper troposphere and lower stratosphere regions [13]. Previous studies have proven the feasibility of using the GRO technique for observing atmospheric parameters, such as refractivity, temperature, water vapor, and pressure for improving numerical weather prediction and global climate monitoring [14–19].

Although GRO has demonstrated some remarkable capabilities, it is limited by the frequencies (1–2 GHz) chosen specifically to minimize its interaction with the atmosphere [2,20]. Three important limitations of GRO are as follows: (1) its inability to separate the temperature and water vapor contributions to refractivity [6]; (2) its insensitivity to water vapor in the colder regions of the troposphere and stratosphere [8]; and (3) the ionospheric error in the retrievals, which is significant at upper stratospheric altitudes [13,21]. In moist air conditions, there is a temperature–humidity ambiguity problem in the middle and low troposphere [19,22]. If the water vapor is neglected in the retrieval procedure, a cold temperature bias will be the result [23]. It is impossible to retrieve water vapor profiles from the refraction measurements unless they are combined with additional temperature observations or model analysis data. In contrast, a temperature deviation of 1–2 K can induce a water vapor pressure retrieval error of 0.2–0.3 hPa [24]. The retrieval accuracy is highly also dependent on the initial model field and model error since different model data have their intrinsic systematic biases, so using different climatology data as the background field can lead to different results [25–27].

The LMO technique uses frequencies near the 22.23 GHz and 183.31 GHz water lines to measure the refraction and absorption of the signals, enabling simultaneous retrieval of the temperature and water vapor profiles without an auxiliary background field [2,3], overcoming the temperature–humidity ambiguity problem of GRO. Furthermore, LMO also has the unique characteristics of radio occultation, high accuracy, high vertical resolution, self-calibration, being able to be used in nearly all-weather, global coverage, and long-term stability [18,28]. Since the LMO concept was proposed, many significant retrieval technique studies have been carried out, focusing mainly on measurement theory, simulation analysis, load development, principle prototype experiments, and so on [29–31]. However, there is still currently no LEO-LEO occultation mission in space. To realize space exploration involving an early LMO mission, a lot of research is still needed.

The LEO-LEO cross-link radio occultation uses the cm and mm wavelengths to monitor attenuation and refraction measurements. The retrieval of LEO-LEO radio occultation is more complicated than GNSS to LEO radio occultation because the attenuation measurements are used in the retrieval [32]. The possibilities and advantages of the LMO technique still need to be investigated. Additionally, each satellite will have transmitter and receiver capabilities, carrying the cm- and mm-wavelength transmitters on one end and the corresponding receivers on the opposite end [6,8]. Therefore, the correct choice of cross-link frequencies is crucial for LMO. In this study, some simulations were performed to analyze the attenuation properties at different heights of cm and mm wavelengths within the 22.23 GHz and 183.31 GHz lines. The LMO signal propagation characteristics were assessed and compared with GRO. Moreover, the retrieval performance of LMO to detect temperature and water vapor profiles using different frequency combinations at the X, K, and M bands was analyzed.

This paper is arranged as follows. Section 2 presents the principles and methods. Section 2.1 introduces the measurement theory. Section 2.2 describes the double differential absorption approach. Section 2.3 describes the forward propagation model. Section 3 illustrates the results of this research, and discussions are given in Section 4. Finally, a conclusion is given in Section 5.

2. Principles and Methods

2.1. Measurement Theory

The LMO technique uses an occultation geometry with transmitter and receiver satellites on the low Earth orbit. Since the transmitters and receivers are independent, the system is referred to as bistatic radar [28,31]. Figure 1 shows a schematic view of microwave occultation links between LEO satellites. When two LEO satellites move to either side of the Earth, microwave signals transmitted by one of the LEO satellites, the transmitter satellite, are refracted and absorbed as they traverse to the atmosphere and are finally received by the LEO receiver on the other LEO satellite [28]. Owing to the relative motion between the satellites, the atmosphere is scanned from top to surface or in the opposite directions, and the excess phase and amplitude attenuation at different heights are measured [33]. This process is called a setting or rising occultation event. The moist atmospheric parameter profiles can be derived from the refraction and attenuation measurements at the receiver. The orbit altitudes of the LMO transmitter and receiver satellites are generally in the range of 300–900 km [3].

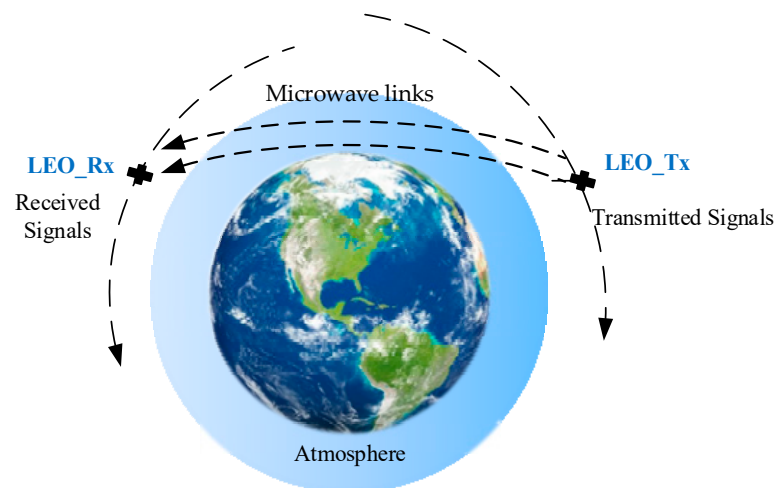


Figure 1. Schematic view of microwave occultation links between LEO satellites.

In the microwave region below 200 GHz, there are two major water vapor absorption lines at 22.23 GHz and 183.31 GHz, which are sensitive to both refraction and absorption [20]. The atmospheric medium will affect both the propagation speed and the amplitude of LMO signals via refraction, scattering, and absorption. Therefore, the refractivity is expressed in a complex form, as follows: $N_c = N' + N''i$, where N' is real refractivity, N'' is imaginary refractivity, and i is an imaginary unit [8].

When the LMO radio signals traverse the atmosphere, the real refractivity causes bending of the ray. The bending angle describes the change in the ray path direction accumulated along the ray path [18]. Assuming spherical symmetry of the atmosphere, the bending angle α as a function of the impact parameter a can be derived via the Doppler shift from the excess phase [34]. The real refractive index n' as a function of height can be converted from the bending angle via the classical Abel transform [28,35]. The bending angle and real refractive index are expressed as follows:

$$\begin{cases} \alpha(a_j) = 2a_j \int_{r_j}^{\infty} \frac{1}{\sqrt{r^2 \cdot (n')^2 - a_j^2}} \frac{d \ln(n')}{dr} dr \\ n'(a_j) = \exp \left(\frac{1}{\pi} \int_{a_j}^{\infty} \frac{\alpha(a)}{\sqrt{a^2 - a_j^2}} da \right) \end{cases}, \quad (1)$$

where the impact parameter $a = r \cdot n'(a) \sin \theta$, and r is the radial distance from the center of the Earth, and θ is the angle between the transmitter and the receiver position vector.

Meanwhile, the intensity I is reduced by absorption along the signal path as $dI = -IkdI$, where l is distance and k is the extinction coefficient [20]. For each LMO radio signal, the observed intensity I is related to the vacuum intensity I_0 . The transmission is defined as $T = I/I_0 = \exp(-\tau)$, where τ is the optical depth. Since intensity is proportional to amplitude A squared ($I \propto A^2$) [3,6], transmission can be computed as a function of the impact parameter can be computed from the amplitude at each signal frequency f_i . In addition, the absorption coefficient can be derived as a function of height from transmission via another Abel transform [2]. The transmission and absorption coefficients are expressed as follows:

$$\begin{cases} T_i(a_j) = \exp\left(-2 \int_{r_j}^{\infty} k_i \frac{n'r}{\sqrt{(n'r)^2 - (n'r_j)^2}} dr\right) \\ k_i(z_j) = \frac{1}{\pi} \left| \frac{da}{dr} \right|_{a=a_j} \int_{a_j}^{\infty} \frac{d \ln T_i(a)}{da} \frac{1}{\sqrt{a^2 - a_j^2}} da \end{cases}, \quad (2)$$

where z_j is the ellipsoidal height level, $z_j = r_j - R_C$, and R_C is the radius of the local curvature [28]. The real refractivity and imaginary refractivity as a function of height can be obtained from the following expressions:

$$\begin{cases} N'(z_j) = 10^6 (n'(a_j) - 1) \\ N''_i(z_j) = 10^6 \cdot \frac{c}{4\pi f_i} k_i(z_j) \end{cases}, \quad (3)$$

where c is the speed of light.

The relationship between the atmospheric state variables and the real refractivity can be expressed using the Smith and Weintraub equation, as follows [3]:

$$N'(z) = 77.6 \frac{p(z)}{T(z)} + 3.73 \times 10^5 \frac{e(z)}{T(z)^2}, \quad (4)$$

where T is temperature, p is pressure, and e is water vapor pressure.

In the case of dry air, where water vapor can be neglected, refractivity is only related to pressure and temperature. Using the refractivity equation together with the ideal gas equation and the hydrostatic equation, pressure, temperature and density profiles can be calculated [36]. In the case of moist air, the contributions from water vapor cannot be neglected. Combining the imaginary refractivity profiles at multiple signal frequencies with the real refractivity profile, together with the hydrostatic equation and the equation of state in moist air, there are at least four equations which can be used to derive the desired parameters pressure, temperature, and water vapor [28]. Additionally, in the case of clouds, there is one additional unknown, namely the cloud liquid water content. Therefore, we will require at least one frequency more than we require in clear sky conditions to distinguish the contributions of water vapor and cloud liquid water to absorption [20].

As the equations are nonlinear, an iterative least-squares optimal estimation method is used to solve the solution at each integration step [37]. For more detailed information about the solution process, please refer to Refs. [23,28].

2.2. Double Differential Absorption Approach

The LMO technique is self-calibrating and eliminates long-term drift [2,3]. These capabilities will meet key needs for climate change monitoring. Furthermore, LMO achieves its unique performance via a double differential absorption approach by measuring signal strength at several frequencies simultaneously [6]. First, amplitude measurement is the change in signal amplitude over an occultation relative to the amplitude measured above the atmosphere where there is no absorption [8]. Second, the amplitudes of two or more

frequencies are simultaneously measured during each occultation, taking the ratio of the amplitudes of signals with similar frequencies to eliminate unwanted common noise and atmospheric effects [8]. The main frequency is near the water vapor absorption line center to measure the strong signal absorption. The calibration frequency is far away from the absorption line center to offset unnecessary effects, such as defocusing and diffusion [2,20].

To obtain the transmission only caused by absorption, the differential transmission between adjacent frequencies is computed. The formula for calculating the differential transmission is as follows [3]:

$$\Delta T(a_j) = T_k^{\log}(a_j) - T_i^{\log}(a_j), k = i + 1, \quad (5)$$

where T_i^{\log} is the transmission in logarithmic form in units of dB. Then, the differential absorption coefficient can be derived from the differential transmission.

2.3. Forward Propagation Model

The original variables of occultation measurement are phase delay and amplitude attenuation of signals. Currently, there is no LEO-LEO occultation mission in space. To study the detection capability of LMO, the excess phases and amplitude attenuations of LMO signals when they pass through the ionosphere and neutral atmosphere and arrive at the receiver satellite were simulated. In this study, the geometric optics method was used for bending angle and transmission retrieval. High-precision 3D ray tracing was used to calculate the refracted ray path, and the millimeter wave propagation model (MPM93) was also used to calculate the absorption loss along the ray path. To retrieve the temperature and water vapor profiles, the LMO measurement errors were added to the excess phases and amplitude attenuations, including the satellite position and velocity error, clock error, local multipath error of receiver antenna, 1/f amplitude noise error and the amplitude drift error.

The ray tracing technique is commonly used for calculating the propagation paths of an electromagnetic signal in a medium specified by a position-dependent refractive index field [13]. Under geometric optical approximation, 3D ray tracing determines the signal propagation path by shooting a target. This method is suitable for signal propagation in the ionosphere and upper atmosphere and has become a significant tool for investigating signal propagation in RO technology [2,3]. The MPM model is used to simulate the atmospheric attenuation coefficient, delay effect, and complex refractive index of frequencies within the range 1–1000 GHz [38]. A detailed description of the absorption due to water vapor and oxygen is given in Ref. [39].

3. Results

3.1. Signal Attenuation Properties

3.1.1. Transmission Profiles

The transmission measurements reveal the attenuation change in signal strength during an occultation epoch. Figure 2 shows the transmission profiles of several frequencies at 22.23 GHz and 183.31 GHz lines in clear sky conditions for two LMO occultation events representative of tropical (Tro) and mid-latitude (Mid) atmosphere. The range is from the near-surface to the lower stratosphere (~25 km), including one millimeter waveband (178–185 GHz) and two centimeter wavebands (23–30 GHz and 9–22.23 GHz), each with eight frequencies. As seen in Figure 2, for the same transmission, the altitude is higher for the tropical atmosphere compared with the mid-latitude because of the more significant amounts of water vapor.

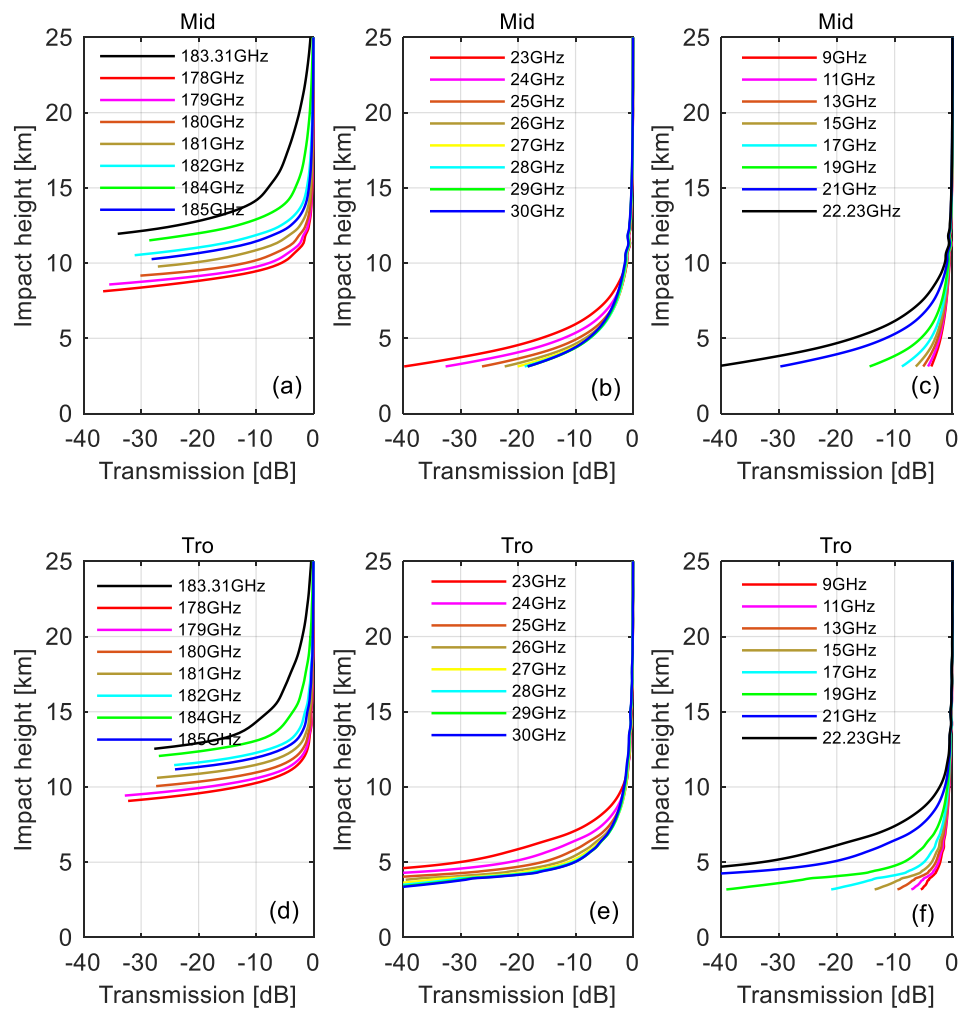


Figure 2. Transmission profiles at several frequencies in clear sky conditions. (a,b,c) are for the mid-latitude (Mid) atmosphere; (d,e,f) are for the tropical (Tro) atmosphere.

For the 178–185 GHz band, the transmission profiles in Figure 2a,d are mainly distributed over 10 km, significantly higher than the 23–30 GHz in Figure 2b,e and the 9–22.23 GHz in Figure 2c,f. Below about 10 km, where moisture is abundant, these millimeter wave signals are almost completely absorbed by the atmosphere, making them undetectable by receivers. Above about 10 km, where moisture is rare, these signals have a strong absorption effect. They are very sensitive to the atmosphere at different altitudes, so they can be used to detect water vapor information in the upper troposphere. For the 23–30 GHz and 9–22.23 GHz bands, these centimeter wave signals are nearly completely transmitted to the atmosphere above about 10 km, which cannot detect effective water vapor information. Below about 10 km, the signals at 23–30 GHz in Figure 2b,e are slightly sensitive to the atmosphere at different altitudes, especially in the tropics below 5 km. The absorption effects of the signals at 9–22.23 GHz in Figure 2c,f differ significantly with altitude. Because of the strong absorption effect, the sensitivity of the signals at 17–22.23 GHz decreases below 5 km, so they can be used to detect water vapor information in the middle troposphere. The signals at 9–15 GHz are sensitive to the atmosphere below 5 km, and so are suitable for exploring the low troposphere.

The 183.31 GHz line is used at altitudes where there is little cloud liquid water content. Thus, Figure 3 only gives the transmission profiles of several frequencies at the 22.23 GHz line in cloudy conditions, including two centimeter wavebands of 23–30 GHz and 9–22.23 GHz. In the mid-latitudes, a cloud layer with a thickness of 0.5 km was set near 4.5 km, and the cloud liquid water content was 0.40 g/m^3 . In the tropics, a cloud

layer with a thickness of 0.8 km was set near 3.5 km, and the cloud liquid water content was 0.60 g/m^3 . As seen in Figure 3a,c, the signals at 23–30 GHz are completely absorbed below 5 km, which can make them undetectable by receivers. The signals at 9–17 GHz in Figure 3b,d are obviously attenuated, and the transmission profiles curve due to the clouds. In addition, compared with 9–17 GHz, the signals at 23–30 GHz are more attenuated by the clouds and affected by scattering due to their shorter wavelengths. Therefore, the signals at 9–17 GHz are generally selected to detect and distinguish the contributions of water vapor and cloud liquid water to absorption in the low and middle troposphere.

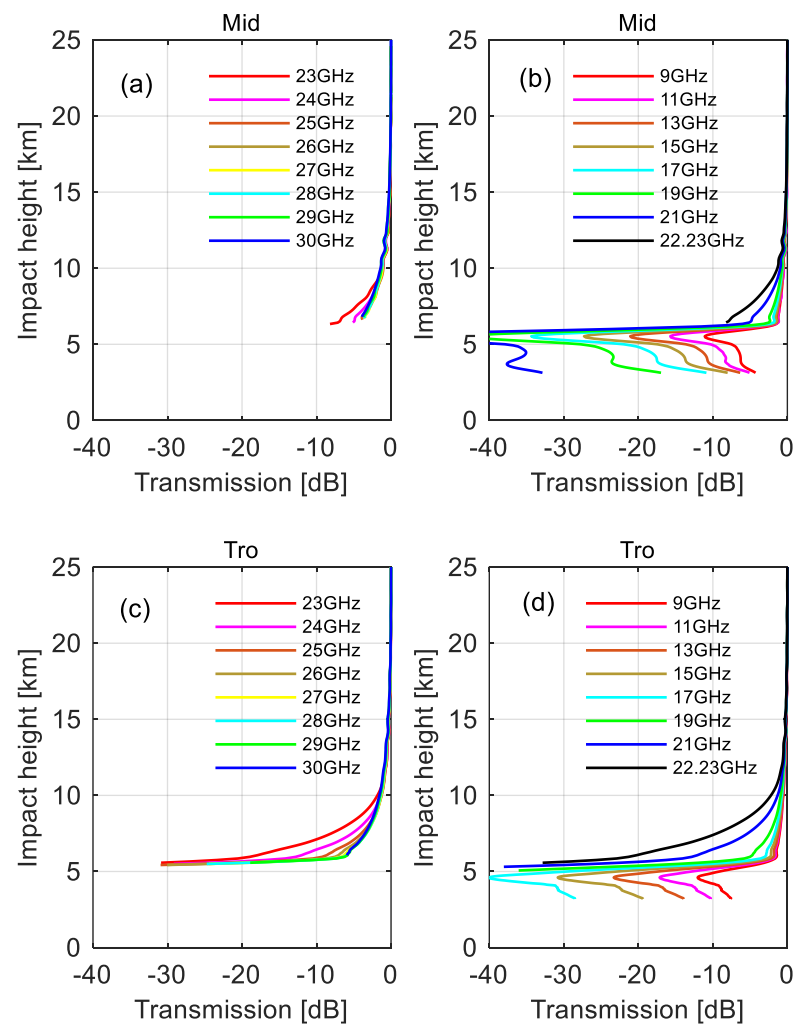


Figure 3. Transmission profiles at several frequencies in cloudy conditions. (a,b) are for the mid-latitude (Mid) atmosphere; (c,d) are for the tropical (Tro) atmosphere.

The above results illustrate that we cannot use a single frequency to cover the water vapor distribution from the near-surface to the lower stratosphere. By using several appropriate frequencies within both the 22.23 GHz and 183.31 GHz lines, we can detect water vapor information over a wide range of altitudes.

3.1.2. Ratio of Frequency Pair

The differential absorption coefficient profile is retrieved from the differential transmission profile of two adjacent frequencies. Figure 4 shows the absolute and differential absorption coefficient profiles and their retrieval errors for two frequency pairs, as follows: 22.23 GHz and 20 GHz, and 17 GHz and 9 GHz. The retrieval errors of the absolute absorption coefficient of each pair below 10–15 km and 7 km show an obvious increase. After taking the ratio of the two frequencies, the retrieval errors of the differential absorption

coefficient largely decrease. The effects of defocusing and diffraction are obviously removed by taking the ratio.

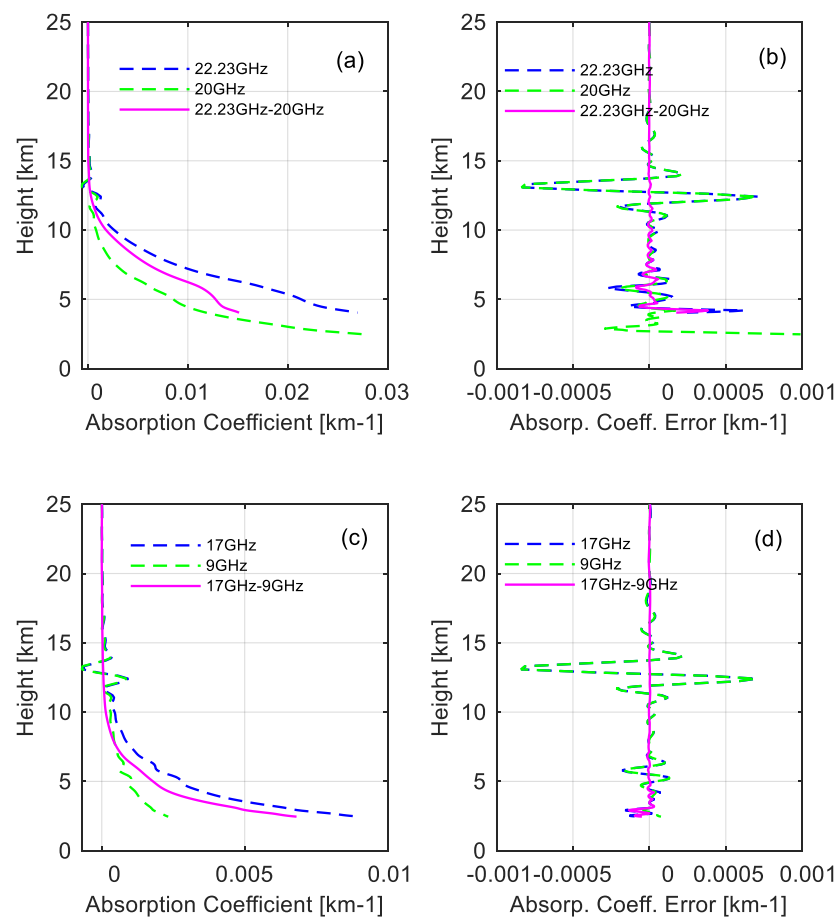


Figure 4. Absolute absorption coefficient and differential absorption coefficient profiles and their retrieval errors. (a,b) are for the frequency pair of 22.23 GHz and 20 GHz; (c,d) are for the frequency pair of 17 GHz and 9 GHz.

The above results illustrate that at least two frequencies are required to generate one absorption coefficient difference under clear sky conditions. In the presence of clouds, three frequencies must be used to generate two absorption coefficient differences.

3.2. Signal Propagation Comparison with GRO

In order to assess the signal propagation characteristics of LMO, five frequencies near the 22.23 GHz and 183.31 GHz absorption lines were selected, including the centimeter wave at the X and K bands, and millimeter wave at the M band. For comparison, the signal propagation of GRO was also simulated. The transmitter frequencies of GRO were the two fixed decimeter waves at the L-band. The detailed frequencies of GRO and LMO are shown in Table 1.

Figure 5a shows how the impact height of the GRO and LMO occultation tangent points varies with time. The occultation events time of GRO and LMO lasts 47.2 s and 37.1 s, respectively. The slope of the LMO profile is steeper than that of GRO. The LMO technique scans the atmosphere from the surface to about 80 km sooner than GRO. Figure 5b,c show the excess phase and amplitude profiles of GRO and LMO. The impact height goes from the near-surface to the stratopause (~50 km). As can be seen, the excess phase in Figure 5b is independent of frequency and increases with a decrease in height. The excess phases of GRO and LMO from about 20 km to 50 km are less than 67.3 m and 62 m, respectively. Atmospheric refraction is obvious below 20 km. The excess phase increases sharply in

the lower troposphere, reaching the maximum of 781 m and 492 m near the surface, respectively. In Figure 5c, the amplitude profiles of GRO at 1.2276 GHz and 1.5754 GHz almost overlap and attenuate very little, within 49 dB. The amplitude profiles of LMO at five signal frequencies are obviously different and attenuate strongly. The amplitudes of 182.2 GHz attenuated to 1.82 dB at 10 km and are almost completely attenuated below 10 km. The amplitudes of 179.0 GHz attenuate to 1.13 dB at 8 km. At 9.7 GHz, 17.25 GHz, and 22.6 GHz, the amplitudes attenuate to 47.3 dB, 40.9 dB, and 4.38 dB near the surface, respectively. The excess phase of the LMO signals is obviously smaller than that of GRO, and the amplitude attenuation of the LMO signals is much greater than that of GRO.

Table 1. The transmitter signal frequencies of GRO and LMO.

GRO		LMO	
Frequency (GHz)	Wavelength(cm)	Frequency (GHz)	Wavelength(cm)
L1 = 1.5754	19.03	Fre1 = 9.7	3.0906
L2 = 1.2276	24.42	Fre2 = 17.25	1.7379
		Fre3 = 22.6	1.4841
		Fre4 = 179.0	0.1675
		Fre5 = 182.2	0.1648

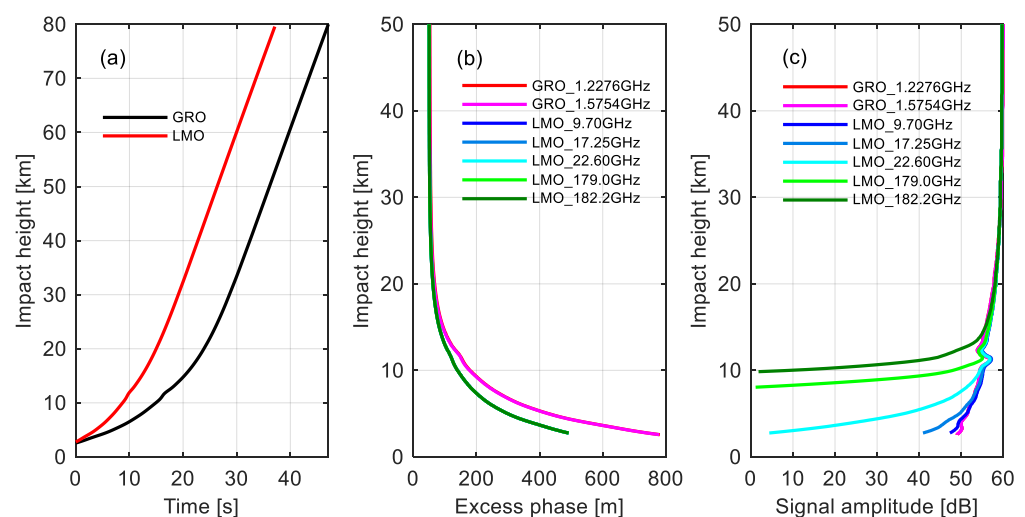


Figure 5. (a) The impact height of the GRO and LMO occultation tangent point varies with time. (b) Excess phase profiles of GRO and LMO. (c) Amplitude profiles of GRO and LMO.

The influence of the ionosphere on the signal propagation of GRO and LMO was compared. Figure 6 shows the bending angle errors of GRO and LMO without ionospheric correction, and the solar activity intensity is low ($F_{10.7} = 80$). Below 35 km, the bending angle errors of GRO and LMO are less than 23.97% and 0.68%, respectively. From about 35 km to 50 km, the bending angle errors of GRO at 1.2276 GHz and 1.5754 GHz increase rapidly, reaching the maximum of 270.85% and 162.84%, respectively. However, the increase in bending angle errors for LMO is still small. The maximum errors at 9.7 GHz, 17.25 GHz, and 22.6 GHz are 5.62%, 1.96%, and 1.22%, respectively, which is about two orders of magnitude smaller than those of GRO. The maximum errors at 179.0 GHz and 182.2 GHz are 0.296% and 0.304%, respectively, which is about three orders of magnitude smaller than those of GRO.

Figure 7 shows the bending angle residual errors of GRO and LMO after ionospheric correction, at impact heights ranging from 30 km to 50 km. The solar activity intensities are low ($F_{10.7} = 80$), medium ($F_{10.7} = 140$), and high ($F_{10.7} = 200$), respectively. As seen in Figure 7a,b, the stronger the solar activity intensity, the larger the ionospheric residual error of GRO. Under $F_{10.7} = 200$, the relative and absolute residual errors of GRO reach

their maximum of -8% and $-5.59 \mu\text{rad}$, respectively. However, the ionospheric residual errors of LMO in Figure 7c,d are very small and vary only slightly with an increase in solar activity intensity. The relative and absolute residual errors of LMO are within $\pm 0.89\%$ and $0.53 \mu\text{rad}$, respectively. The bending angle residual ionospheric error of GRO is still larger than that of LMO by about one order of magnitude even after ionospheric correction.

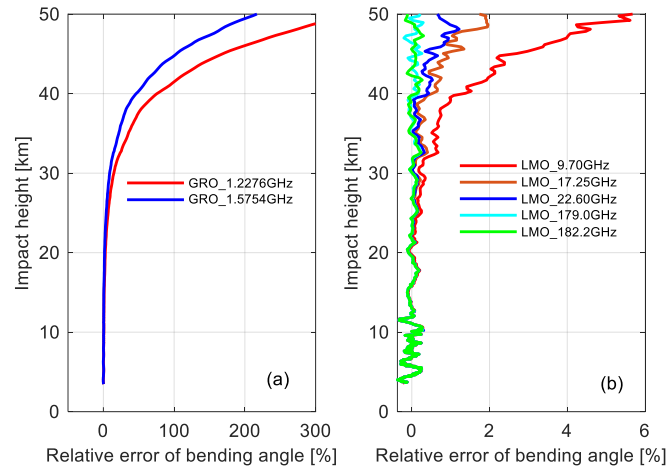


Figure 6. Bending angle error profiles without ionospheric correction. (a) is for GRO; (b) is for LMO.

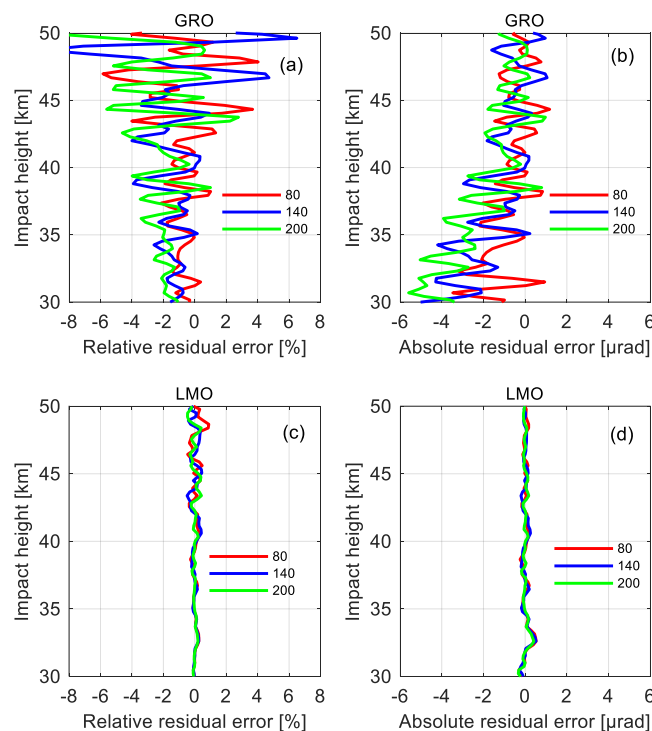


Figure 7. The ionospheric residual error of bending angle profiles after ionospheric correction. (a,b) are for GRO; (c,d) are for LMO.

3.3. Detection Performance of Different Frequency Combinations

3.3.1. Frequencies Setting

In order to assess the performance of LEO-LEO microwave occultation to detect temperature and water vapor profiles using the centimeter and millimeter waves, a series of simulation retrieval experiments were carried out. According to the above results, 22.6 GHz and 182.2 GHz were selected as the main detection frequencies of the 22.23 GHz low band and 183.31 GHz high band, respectively. Different reference detection frequencies

were selected to form eight groups of frequency combinations, including four groups in the K band, two groups in the X and K bands, and two groups in the X, K, and M bands. The detailed frequency combination settings are given in Table 2.

Table 2. Different frequency combinations settings.

Group	Wavelength	Band	Frequencies (GHz)	Number of Frequencies
fre01	Centimeter wave	K	20.2, 22.6	2
fre02	Centimeter wave	K	17.25, 22.6	2
fre03	Centimeter wave	K	20.2, 20.8, 22.6	3
fre04	Centimeter wave	K	17.25, 20.2, 22.6	3
fre05	Centimeter wave	X+K	9.7, 17.25, 22.6	3
fre06	Centimeter wave	X+K	9.7, 13.5, 17.25, 20.2, 22.6	5
fre07	Centimeter and millimeter wave	X+K+M	9.7, 17.25, 22.6, 179.0, 182.2	5
fre08	Centimeter and millimeter wave	X+K+M	9.7, 17.25, 22.6, 179.0, 181.3, 181.9, 182.2	7

3.3.2. K Band

Figure 8 shows the retrieval errors of temperature profiles at the K band. Using only two frequencies (fre01 and fre02) at the K band, in the clear conditions, the RMS (root mean square) errors at about 5–50 km are almost within 2 K. From 7 km to 40 km, the retrieval accuracy is better. The mean bias is almost within ± 0.3 K. The RMS errors are less than 1 K. Above about 40 km, the retrieval errors of fre01 and fre02 increase obviously, and the former is greater than the latter because the reference frequency of 20.2 GHz of fre01 is closer to the main frequency of 22.6 GHz than the 17.25 GHz of fre02. Below about 7 km, the retrieval errors of fre01 and fre02 are similar, and both increase significantly. The RMS errors below about 5 km exceed 2 K. In cloudy conditions, there is one additional variable, namely the cloud liquid water content. The temperature profiles of fre01 and fre02 below about 8 km cannot be effectively retrieved because there is only one differential transmission profile after differential processing.

Using three frequencies (fre03 and fre04) at the K band, the retrieval accuracy of fre04 above about 40 km is improved compared with fre01 and fre02. The RMS errors are less than 1.5 K. However, the retrieval errors of fre03 are larger than those of fre01 and fre02, because the reference frequency of 20.8 GHz of fre03 is closer to the main frequency than the 20.2 GHz of fre01. Below about 7 km, the retrieval errors of fre03 and fre04 are significantly smaller than those of fre01 and fre02, and the RMS errors above about 2.5 km are mostly within 2 K, since the three frequencies can obtain more absorption information than the two frequencies of fre01 and fre02. In cloudy conditions, the temperature profile below 8 km can be effectively retrieved, but the RMS error below about 6 km increases significantly exceeds 2 K, and cannot, therefore, meet the detection requirements [40].

Figure 9 shows the retrieval errors of water vapor profiles at the K band. Using only two frequencies (fre01 and fre02) at the K band, in the clear conditions, the RMS errors are mostly within 10% from 5 km to 15 km. The retrieval errors of fre01 and fre02 above 15 km increase obviously, and the former increase faster than the latter. Above about 17 km, the RMS errors are more than 20%, which cannot meet the detection requirements. Below about 5 km, the retrieval errors of fre01 and fre02 are similar, and both increase significantly, with the RMS errors below about 4 km exceeding 20%. In cloudy conditions, the water vapor profile below about 8 km cannot be effectively retrieved. Using three frequencies (fre03 and fre04) at the K band, the retrieval accuracy above about 15 km is not improved, but it is improved below about 5 km. The retrieval error of fre04 is smaller than those of fre01 and fre02, and the RMS errors exceeding 20% are only below about 2.5 km. In cloudy conditions, the water vapor profile below 8 km can be effectively retrieved, but the RMS errors of fre03 below 6 km and fre04 below 4 km begin to increase significantly, exceeding 20%, which cannot meet the detection requirements.

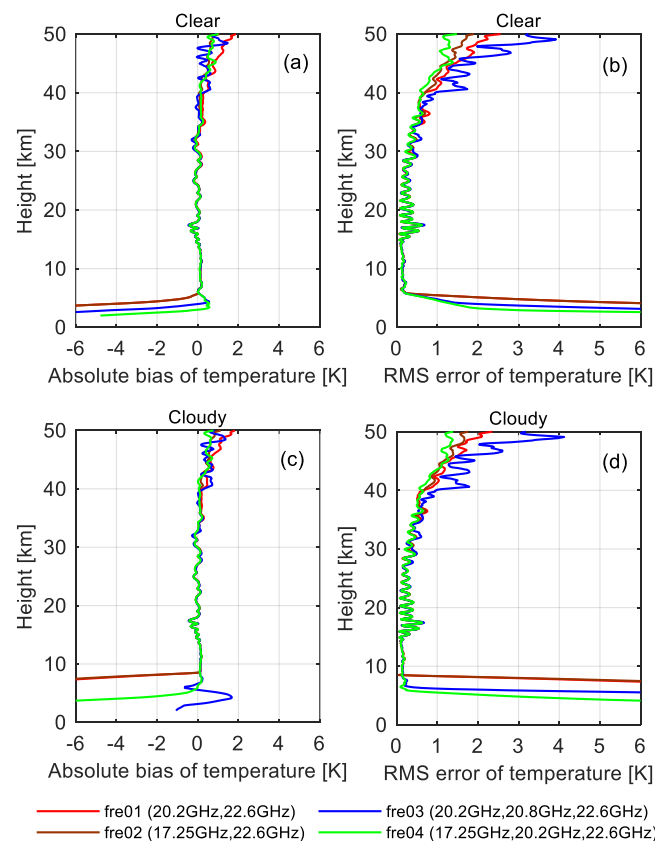


Figure 8. Retrieval errors of temperature profiles at the K band. (a,b) are in clear condition; (c,d) are in cloudy conditions.

3.3.3. X+K Band

Figure 10 shows the retrieval errors of temperature profiles at the X+K band. In the clear conditions, at about 2.5–50 km, the mean bias is mostly within ± 1 K, and the RMS errors are less than 1.5 K. The retrieval accuracy is even better at about 7–40 km, where the mean bias is mostly within ± 0.3 K, and the RMS errors are less than 0.5 K. In the cloudy conditions, the RMS errors of fre05 below about 5 km increase significantly, exceeding 2 K. Compared with fre05, the retrieval accuracy of fre06 is significantly improved, and the RMS errors are more than 2 K only below about 2.5 km. Figure 11 shows the retrieval errors of water vapor profiles at the X+K band. In the clear conditions, the RMS errors at about 2.5–15 km are mostly within 5%. The retrieval errors increase obviously above about 17 km, and the RMS errors rapidly exceed 20%. In cloudy conditions, the RMS errors of fre05 increase significantly below about 5 km and exceed 20% below about 4 km, which cannot meet the detection requirements. Compared with fre05, the retrieval accuracy of fre06 is significantly improved, and the RMS errors are less than 5% at about 2.5–5 km. This is because fre06 has two more frequencies than fre05, allowing it to obtain more absorption information.

3.3.4. X+K+M Band

Figure 12 shows the retrieval errors of temperature profiles and water vapor profiles at the X+K+M band. At about 2.5–50 km, the temperature mean bias is mostly within ± 1 K, and the RMS errors are less than 1.5 K. The water vapor RMS errors at about 2.5–24 km are less than 10%. Compared with the X+K band, also using the frequencies at the M-band, the water vapor retrieval accuracies of fre07 and fre08 above 15 km are significantly improved, while the temperature retrieval accuracies are slightly improved. Furthermore, it can be determined that the temperature and water vapor profiles retrieved by fre08 show a sharp error bump at about 12–14 km, especially for temperature, with the RMS errors even

reaching 4 K. This is because fre08 has two more frequencies at the M-band than fre07, but the current retrieval algorithm has an unreasonable role in the weight distribution of the frequencies, which needs to be improved and optimized in the future.

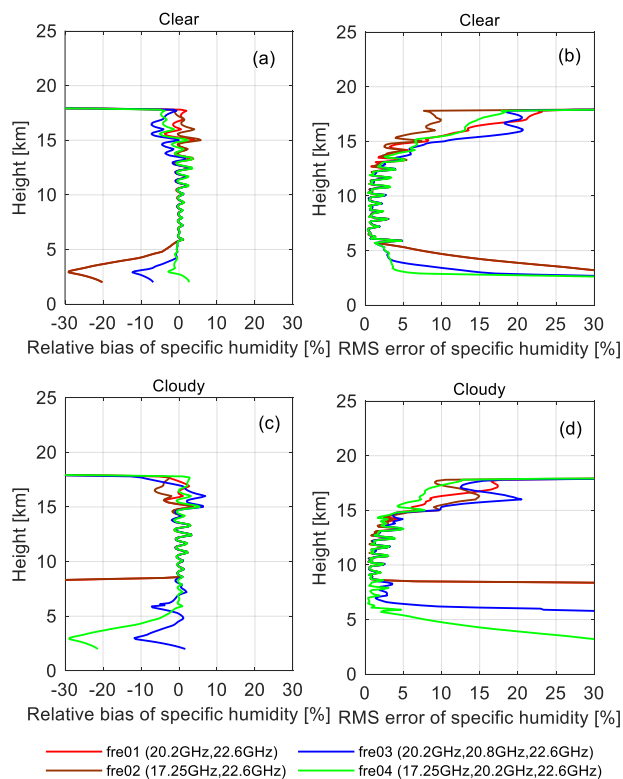


Figure 9. Retrieval errors of water vapor profiles at the K band. (a,b) are in clear condition; (c,d) are in cloudy conditions.

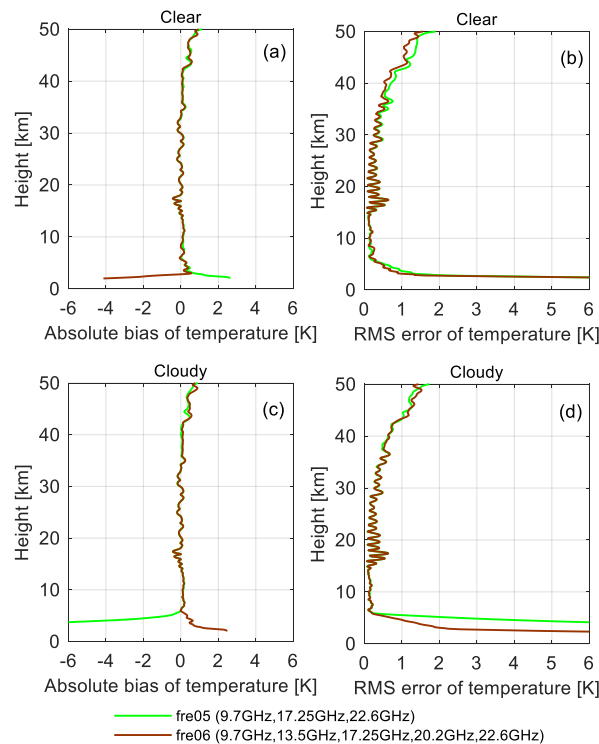


Figure 10. Retrieval errors of temperature profiles at the X+K band. (a,b) are in clear condition; (c,d) are in cloudy conditions.

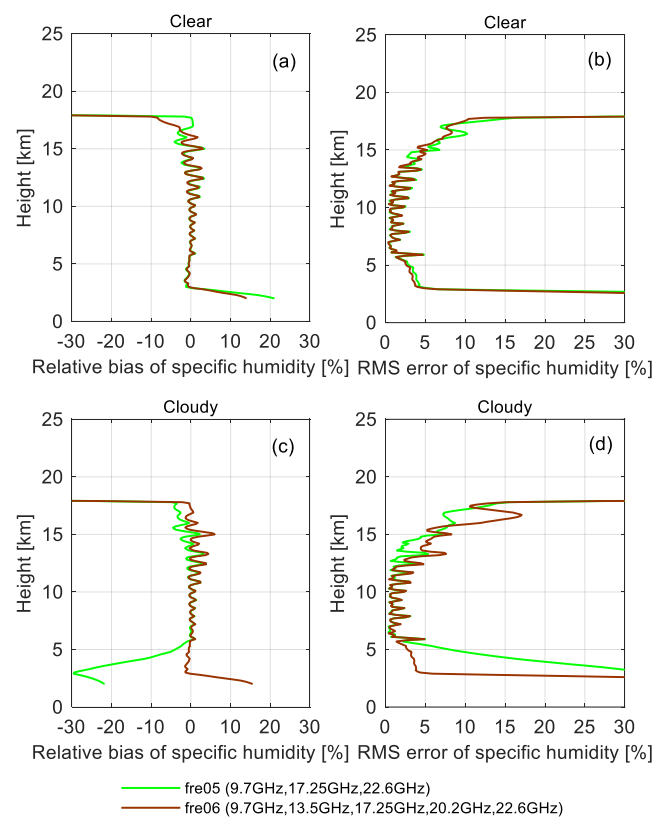


Figure 11. Retrieval errors of water vapor profiles at the X+K band. (a,b) are in clear conditions; (c,d) are in cloudy conditions.

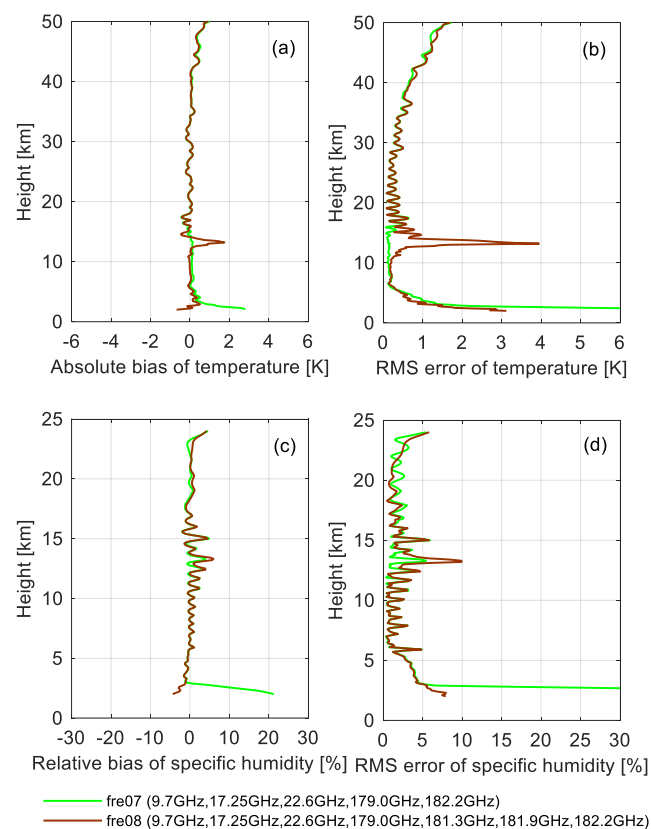


Figure 12. Retrieval errors of temperature (a,b) and water vapor (c,d) profiles at the X+K+M band.

4. Discussion

The LMO study indicates that attenuation measurements used along with the standard refraction measurements greatly extend the capabilities of the radio occultation technique. As shown in Figures 2 and 3, by using several appropriate frequencies within both the 22.23 GHz and 183.31 GHz lines, water vapor information can be detected from the near-surface to the lower stratosphere, and the absorption of cloud liquid water can also be distinguished. By taking the ratio of two adjacent frequencies, the non-absorption effects in the atmosphere are obviously removed. Section 3.2 shows that the ionosphere has a small influence on LMO signals. The LMO technique can improve the bending angle retrieval accuracy above 35 km compared with GRO.

The detection performance of LMO temperature and water vapor profiles is related to the frequency combinations used. In Section 3.3, when using only two frequencies at the K band, in the clear conditions, the temperature profiles at about 5–50 km and water vapor profiles at about 5–15 km can be accurately detected. However, in cloudy conditions, the temperature profiles and water vapor profiles below about 8 km cannot be effectively retrieved. When using three frequencies at the K band, in clear conditions, the retrieval accuracies of temperature and water vapor at about 2.5–5 km are obviously improved. In cloudy conditions, the temperature profiles and water vapor profiles below about 8 km can be effectively retrieved, but the retrieval errors below 6 km are too large to meet the detection requirements. When using several frequencies at the X+K band, in clear conditions, the temperature profiles at about 2.5–50 km and water vapor profiles at about 2.5–15 km can be accurately detected. In the cloudy conditions, using the frequency set of 9.7 GHz, 13.5 GHz, 17.25 GHz, 20.2 GHz, and 22.6 GHz, the retrieval accuracies of the temperature profiles and water vapor profiles at about 2.5–5 km are obviously improved. When using the several frequencies at the X+K+M band, the increased M-band frequencies do not improve the temperature retrieval accuracy but can significantly improve the water vapor retrieval accuracy above about 15 km and increase the detectable height of water vapor to about the lower stratosphere.

In reality, the selected frequency combination needs to comprehensively consider the scientific requirements, the hardware development technology, and the cost [22,40]. If only scientific requirements are considered, in order to obtain the maximum detection accuracy and height range of temperature and water vapor profiles, the frequency combination at the X+K+M band in Section 3.3 should be used. In this case, the satellite platform needs to be equipped with occultation transmitters of 22.23 GHz low band and 183.31 GHz high band, respectively, and the X, K, and M bands each need a receiving antenna, which will greatly increase the technical difficulty and cost of instrument development. At present, the 22.23 GHz low-frequency technology is mature, but the 183.31 GHz high-frequency instrumentation is not, because of the problem of high-frequency oscillators. Therefore, in order to promote the early implementation of an LMO missions in space, a trade-off between scientific requirements and hardware development is needed. In this study, the preferred frequency combination is 9.7 GHz, 13.5 GHz, 17.25 GHz, 20.2 GHz, and 22.6 GHz at the X+K band, which can accurately detect the temperature profiles at about 2.5–50 km and water vapor profiles at about 2.5–15 km under clear and cloudy conditions.

It is worth noting that temperature and water vapor retrieval errors below 2.5 km increase significantly even when using the X band frequencies. In the simulation experiments, this is partly caused by the topography and partly due to multipath effects in the lower troposphere limiting the ray-tracing in the forward modelling [28]. An optimized retrieval algorithm is needed to make a more reasonable weight distribution of the frequencies and to reduce the retrieval errors in the lower troposphere. In addition, Kursinski et al. suggested using one or more lower frequencies between 2 and 5 GHz to reduce the near-surface temperature uncertainty in the tropics [8]. Its feasibility and detection performance need to be further studied and verified in the future work.

5. Conclusions

In this study, some simulations were performed to assess the detection performance of LMO. The results illustrate that LMO can greatly extend the capabilities of the radio occultation technique. Indeed, LMO may improve the bending angle retrieval accuracy above 35 km compared with GRO. By using several appropriate frequencies at the X+K+M band, water vapor profiles from the near-surface to the lower stratosphere (~24 km) can be obtained. The LMO method achieves its unique performance via a double differential absorption approach. When using only two frequencies at the K band, the retrieval accuracies of temperature and water vapor at about 2.5–5 km are obviously improved in clear conditions. However, the temperature profiles and water vapor profiles below about 8 km cannot be effectively retrieved in cloudy conditions. The added X-band frequencies can significantly improve the retrieval accuracy for temperature and water vapor below about 5 km. However, the increased number of M-band frequencies does not improve the temperature retrieval accuracy but can significantly improve the water vapor retrieval accuracy above about 15 km, especially at about 17–24 km, and the RMS errors decrease from over 20% to less than 10%. For promoting the early implementation of an LMO mission in space, a frequency combination of 9.7 GHz, 13.5 GHz, 17.25 GHz, 20.2 GHz, and 22.6 GHz at the X+K band is preferred, which can provide the potential to observe the temperature profiles at about 2.5–50 km and water vapor profiles at about 2.5–15 km accurately under clear and cloudy conditions.

The LEO-LEO cross-link radio occultation method using cm and mm wavelengths provides a potential way to measure the moist atmospheric profiles, which is an important supplement to the other atmospheric detection methods. More in-depth research involving theoretical studies and hardware development is still required to improve LMO detection capability. An optimized retrieval algorithm is needed to ensure a more reasonable weight distribution of the frequencies and to reduce the retrieval errors of temperature and water vapor profiles below 2.5 km. In recent years, small satellites have been extensively launched into space. The development of the LEO-LEO radio occultation technique can provide essential vertical atmospheric datasets for global climate change research in the future.

Author Contributions: Conceptualization, Z.Z., X.W. and D.L.; methodology, Z.Z., X.W. and D.L.; software, Z.Z.; validation, Z.Z.; formal analysis, Z.Z. and X.W.; writing—original draft preparation, Z.Z.; supervision, D.L.; project administration, X.W.; funding acquisition, D.L. All authors have read and agreed to the published version of the manuscript.

Funding: This research was funded by the Strategic Priority Research Program of the Chinese Academy of Sciences (grant no. XDA15021000, XDA15021001).

Data Availability Statement: Data related to this article are available upon request to the corresponding authors.

Acknowledgments: We acknowledge the radio occultation software development teams at Wegener Center for Climate and Global Change (WEGC).

Conflicts of Interest: The authors declare no conflict of interest.

References

1. Sun, Y. Impact of human activities on climate system: An interpretation of Chapter III of WGI report of IPCC AR6. *Trans. Atmos. Sci.* **2021**, *44*, 654–657.
2. Kursinski, E.R.; Syndergaard, S.; Flittner, D.; Feng, D.; Hajj, G.; Herman, B.; Ward, D.; Yunck, T. A microwave occultation observing system optimized to characterize atmospheric water, temperature, and geopotential via absorption. *J. Atmos. Ocean. Technol.* **2002**, *19*, 1897–1914. [[CrossRef](#)]
3. Schweitzer, S.; Kirchengast, G.; Schwaerz, M.; Fritzer, J.; Gorbunov, M.E. Thermodynamic state retrieval from microwave occultation data and performance analysis based on end-to-end simulations. *J. Geophys. Res. Atmos.* **2011**, *116*, D10301. [[CrossRef](#)]
4. Shine, K.P.; Sinha, A. Sensitivity of the Earth's climate to height dependent changes in the water vapor mixing ratio. *Nature* **1991**, *354*, 382–384. [[CrossRef](#)]
5. He, Y.; Zhu, X.; Sheng, Z.; He, M.; Feng, Y. Observations of Inertia Gravity Waves in the Western Pacific and Their Characteristic in the 2015/2016 Quasi-biennial Oscillation Disruption. *J. Geophys. Res. Atmos.* **2022**, *127*, e2022JD037208. [[CrossRef](#)]

6. Ward, D.M.; Kursinski, E.R.; Otarola, A.C.; Stovern, M.; McGhee, J.; Young, A.; Hainsworth, J.; Hagen, J.; Sisk, W.; Reed, H. Retrieval of water vapor using ground-based observations from a prototype ATOMMS active centimeter- and millimeter-wavelength occultation instrument. *Atmos. Meas. Tech.* **2019**, *12*, 1955–1977. [[CrossRef](#)]
7. Ji, Q.; Zhu, X.; Sheng, Z.; Tian, T. Spectral Analysis of Gravity Waves in the Martian Thermosphere during Low Solar Activity Based on MAVEN/NGIMS Observations. *Astrophys. J.* **2022**, *938*, 97. [[CrossRef](#)]
8. Kursinski, E.R.; Ward, D.M.; Otarola, A.C.; McGhee, J.; Stovern, M.; Sammler, K.; Reed, H.; Erickson, D.; McCormick, C.; Griggs, E. Atmospheric profiling via satellite to satellite occultations near water and ozone absorption lines for weather and climate. In Proceedings of the SPIE 9881, Earth Observing Missions and Sensors: Development, Implementation, and Characterization IV, New Delhi, India, 2 May 2016.
9. Zhang, J.; Ji, Q.Q.; Sheng, Z.; He, M.Y.; He, Y.; Zuo, X.J.; He, Z.F.; Qin, Z.L.; Wu, G.Y. Observation based climatology Martian atmospheric waves perturbation Datasets. *Sci. Data* **2023**, *10*, 9. [[CrossRef](#)]
10. Yunck, T.P.; Hajj, G.A.; Kursinski, E.R.; LaBrecque, J.A.; Lowe, S.T.; Watkins, M.M.; McCormick, C. AMORE: An autonomous constellation concept for atmospheric and ocean observation. *Acta Astronaut.* **2000**, *46*, 355–364. [[CrossRef](#)]
11. Ware, R.; Exner, M.; Feng, D.; Gorbunov, M.; Hardy, K.; Herman, B.; Kuo, Y.; Meehan, T.; Melbourne, W.; Rocken, C.; et al. GPS sounding of the atmosphere from low earth orbit: Preliminary results. *Bull. Am. Meteorol. Soc.* **1996**, *77*, 19–40. [[CrossRef](#)]
12. Hajj, G.A.; Kursinski, E.R.; Romans, L.J.; Bertiger, W.I.; Leroy, S.S. A technical description of atmospheric sounding by GPS occultation. *J. Atmos. Solar-Terr. Phys.* **2002**, *64*, 451–469. [[CrossRef](#)]
13. Liu, C.L.; Kirchengast, G.; Zhang, K.; Norman, R.; Li, Y.; Zhang, S.C.; Fritzer, J.; Schwaerz, M.; Wu, S.Q.; Tan, Z.X. Quantifying residual ionospheric errors in GNSS radio occultation bending angles based on ensembles of profiles from end-to-end simulations. *Atmos. Meas. Tech.* **2015**, *8*, 2999–3019. [[CrossRef](#)]
14. Yunck, T.P.; Liu, C.H.; Ware, R.J. A History of GPS Sounding. *Terr. Atmos. Ocean. Sci.* **2000**, *11*, 1–20. [[CrossRef](#)]
15. Wickert, J.; Reigber, C.; Beyerle, G.; Konig, R.; Marquardt, C.; Schmidt, T.; Grunwaldt, L.; Galas, R.; Meehan, T.K.; Melbourne, W.G.; et al. Atmosphere sounding by GPS radio occultation: First results from CHAMP. *Geophys. Res. Lett.* **2001**, *28*, 3263–3266. [[CrossRef](#)]
16. Ho, S.-p.; Yue, X.; Zeng, Z.; Ao, C.O.; Huang, C.-Y.; Kursinski, E.R.; Kuo, Y.-H. Applications of COSMIC Radio Occultation Data from the Troposphere to Ionosphere and Potential Impacts of COSMIC-2 Data. *Bull. Am. Meteorol. Soc.* **2014**, *95*, ES18–ES22. [[CrossRef](#)]
17. Liu, Z.; Sun, Y.; Bai, W.; Xia, J.; Tan, G.; Cheng, C.; Du, Q.; Wang, X.; Zhao, D.; Tian, Y.; et al. Validation of Preliminary Results of Thermal Tropopause Derived from FY-3C GNOS Data. *Remote Sens.* **2019**, *11*, 1139. [[CrossRef](#)]
18. Kursinski, E.R.; Hajj, G.A.; Schofield, J.T.; Linfield, R.P.; Hardy, K.R. Observing Earth's atmosphere with radio occultation measurements using the Global Positioning System. *J. Geophys. Res. Atmos.* **1997**, *102*, 23429–23465. [[CrossRef](#)]
19. Wang, X.; Lu, D.R. Retrieval of water vapor profiles with radio occultation measurements using an artificial neural network. *Adv. Atmos. Sci.* **2005**, *22*, 759–764. [[CrossRef](#)]
20. Feng, D.D.; Syndergaard, S.; Herman, B.M.; Kursinski, E.R.; Yunck, T.P.; Romberg, F.W. Deriving atmospheric water vapor and ozone profiles from active microwave occultation measurements. *Sens. Syst. Next-Gener. Satell. IV* **2001**, *4169*, 299–308. [[CrossRef](#)]
21. Fu, N.; Guo, P.; Wu, M.; Huang, Y.; Hu, X.; Hong, Z. The Two-Parts Step-by-Step Ionospheric Assimilation Based on Ground-Based/Spaceborne Observations and Its Verification. *Remote Sens.* **2019**, *11*, 1172. [[CrossRef](#)]
22. Liu, C.L.; Kirchengast, G.; Syndergaard, S.; Kursinski, E.R.; Sun, Y.Q.; Bai, W.H.; Du, Q.F. A review of low Earth orbit occultation using microwave and infrared-laser signals for monitoring the atmosphere and climate. *Adv. Space Res.* **2017**, *60*, 2776–2811. [[CrossRef](#)]
23. Herman, B.M.; Feng, D.; Flittner, D.; Kursinski, E.R.; Syndergaard, S.; Ward, D. An overview of the university of Arizona ATOMS project. In *Occultations for Probing Atmosphere and Climate*; Kirchengast, G., Foelsche, U., Steiner, A.K., Eds.; Springer: Berlin/Heidelberg, Germany, 2004; pp. 189–200.
24. Palmer, P.I.; Barnett, J.J.; Eyre, J.R.; Healy, S.B. A nonlinear optimal, estimation inverse method for radio occultation measurements of temperature, humidity, and surface pressure. *J. Geophys. Res. Atmos.* **2000**, *105*, 17513–17526. [[CrossRef](#)]
25. Poli, P.; Joiner, J.; Kursinski, E.R. 1DVAR analysis of temperature and humidity using GPS radio occultation refractivity data. *J. Geophys. Res. Atmos.* **2002**, *107*, 14–20. [[CrossRef](#)]
26. Healy, S.B.; Eyre, J.R. Retrieving temperature, water vapour and surface pressure information from refractive-index profiles derived by radio occultation: A simulation study. *J. Roy. Meteorol. Soc.* **2000**, *126*, 1661–1683. [[CrossRef](#)]
27. Li, Y.; Kirchengast, G.; Scherllin-Pirscher, B.; Schwaerz, M.; Nielsen, J.K.; Ho, S.-p.; Yuan, Y.-b. A New Algorithm for the Retrieval of Atmospheric Profiles from GNSS Radio Occultation Data in Moist Air and Comparison to 1DVar Retrievals. *Remote Sens.* **2019**, *11*, 2729. [[CrossRef](#)]
28. Schweitzer, S. Atmosphere and Climate Explorer mission ACE+: Humidity and temperature retrieval performance analysis. Master's Thesis, Institute for Geophysics Astrophysics and Meteorology, University of Graz, Graz, Austria, 2004.
29. Kirchengast, G.; Schweitzer, S. Climate benchmark profiling of greenhouse gases and thermodynamic structure and wind from space. *Geophys. Res. Lett.* **2011**, *38*, 142–154. [[CrossRef](#)]
30. Proschek, V.; Kirchengast, G.; Schweitzer, S. Greenhouse gas profiling by infrared-laser and microwave occultation: Retrieval algorithm and demonstration results from end-to-end simulations. *Atmos. Meas. Tech.* **2011**, *4*, 2035–2058. [[CrossRef](#)]

31. Kursinski, E.R.; Ward, D.; Stovorn, M.; Otarola, A.C.; Young, A.; Wheelwright, B.; Stickney, R.; Albanna, S.; Duffy, B.; Groppi, C.; et al. Development and testing of the Active Temperature, Ozone and Moisture Microwave Spectrometer (ATOMMS) cm and mm wavelength occultation instrument. *Atmos. Meas. Tech.* **2012**, *5*, 439–456. [[CrossRef](#)]
32. Benzon, H.H.; Høeg, P. Wave optics-based LEO-LEO radio occultation retrieval. *Radio Sci.* **2016**, *51*, 589–602. [[CrossRef](#)]
33. Kursinski, E.R.; Hajj, G.A.; Hardy, K.R.; Romans, L.J.; Schofield, J.T. Observing tropospheric water-vapor by radio occultation using the global positioning system. *Geophys. Res. Lett.* **1995**, *22*, 2365–2368. [[CrossRef](#)]
34. Fjeldbo, G.; Kliore, A.J.; Eshlemen, V.R. Neutral atmosphere of venus as studied with mariner-v radio occultation experiments. *Astron. J.* **1971**, *76*, 123. [[CrossRef](#)]
35. Syndergaard, S. Modeling the impact of the Earth's oblateness on the retrieval of temperature and pressure profiles from limb sounding. *J. Atmos. Solar-Terr. Phys.* **1998**, *60*, 171–180. [[CrossRef](#)]
36. Li, Y.; Yuan, Y.; Wang, X. Assessments of the Retrieval of Atmospheric Profiles from GNSS Radio Occultation Data in Moist Tropospheric Conditions Using Radiosonde Data. *Remote Sens.* **2020**, *12*, 2717. [[CrossRef](#)]
37. Rodgers, C.D. *Inverse Methods for Atmospheric Sounding: Theory and Practice*; World Scientific Publishing: Singapore, 2000; pp. 43–61.
38. Liebe, H.J. An updated model for millimeter wave-propagation in moist air. *Radio Sci.* **1985**, *20*, 1069–1089. [[CrossRef](#)]
39. Liebe, H.J.; Hufford, G.A.; Cotton, M.G. Propagation modeling of moist air and suspended water/ice particles at frequencies below 1000 GHz. In Proceedings of the NATO/AGARD Wave Propagation Panel, 52nd Meeting, Mallorca, Spain, 17–20 May 1993.
40. Larsen, G.B.; Kirchengast, G.; Bernath, P. *Science Objectives and Observational Requirements of The ACCURATE Mission Concept*; Technical Report DMI/ESA-IRDAS/ObsReq/Oct2009; Danish Meteorology Institute: Copenhagen, Denmark, 2009.

Disclaimer/Publisher's Note: The statements, opinions and data contained in all publications are solely those of the individual author(s) and contributor(s) and not of MDPI and/or the editor(s). MDPI and/or the editor(s) disclaim responsibility for any injury to people or property resulting from any ideas, methods, instructions or products referred to in the content.